Volume 50 Issue 11 NOVEMBER 2010 ISSN 0890-6955

ELSEVIER

INTERNATIONAL JOURNAL OF

MACHINE TOOLS & MANUFACTURE

DESIGN, RESEARCH AND APPLICATION

Editor-in-Chief: T A Dean

Contents of this issue:

Available online at www.sciencedirect.com

ScienceDirect

International Journal of Machine Tools & Manufacture 50 (2010) 943–960

Contents lists available at ScienceDirect

International Journal of Machine Tools & Manufacture

journal homepage: www.elsevier.com/locate/ijmactool

Modified material constitutive models for serrated chip formation simulations and experimental validation in machining of titanium alloy Ti–6Al–4V

Mohammad Sima, Tuğrul Özel *

Manufacturing Automation Research Laboratory, Department of Industrial and Systems Engineering, Rutgers University, Piscataway, NJ 08854, USA

ARTICLE INFO

Article history:
Received 19 June 2010
Received in revised form
7 August 2010
Accepted 9 August 2010
Available online 19 August 2010

Keywords:
Machining
Titanium alloys
Finite element simulations
Flow softening

ABSTRACT

Titanium alloys present superior properties such as high strength-to-weight ratio and resistance to corrosion but, possess poor machinability. In this study, influence of material constitutive models and elastic–viscoplastic finite element formulation on serrated chip formation for modeling of machining Ti–6Al–4V titanium alloy is investigated. Temperature-dependent flow softening based modified material models are proposed where flow softening phenomenon, strain hardening and thermal softening effects and their interactions are coupled. Orthogonal cutting experiments have been conducted with uncoated carbide (WC/Co) and TiAlN coated carbide cutting tools. Temperature-dependent flow softening parameters are validated on a set of experimental data by using measured cutting forces and chip morphology. Finite Element simulations are validated with experimental results at two different rake angles, three different undeformed chip thickness values and two different cutting speeds. The results reveal that material flow stress and finite element formulation greatly affects not only chip formation mechanism but also forces and temperatures predicted. Chip formation process for adiabatic shearing in machining Ti–6Al–4V alloy is successfully simulated using finite element models without implementing damage models.

1. Introduction

Titanium Ti–6Al–4V $\alpha+\beta$ alloy, the most commonly used titanium alloy in aerospace and biomedical industries, exhibits highly favorable properties such as a high strength-to-weight ratio, good heat treatment capability, low density, good bio-compatibility and resistance to corrosion. Titanium Ti–6Al–4V alloy is considered difficult to machine because of its low thermal conductivity, high chemical reactivity with cutting tool materials at elevated temperatures, and low modulus of elasticity even though its annealed hardness is only about 35 HRC [1]. That is because, the heat generated during machining is concentrated at the cutting tool's rake face in addition to the vibrations generated during machining caused by its low modulus of elasticity and serrated chip formation resulting in rapid tool wear and poor workpiece surface quality. Therefore, selecting cutting conditions, tool material and its coating, and cutting edge geometry is important not only to increase the productivity of machining operation but also to obtain a desirable surface integrity (i.e. residual stresses, surface roughness, etc.) of the finished machined part. Hence, comprehensive reviews on machinability of titanium alloys are provided in [1–4].

Many experimental works have been dedicated to understand the chip formation mechanism and its implications in titanium machining. For this purpose, quick-stop tests in orthogonal cutting are often carried out to capture instantaneous chip formation and chip morphology [5,6] or after machining, images of polished and etched chip cross-sections are captured with the help of optical or scanning electron microscopy [4,7–11]. Such chip images depict highly serrated shape with regions of co-existing adiabatic shear bands and cracks (see Fig. 1). These segmented, but continuous, chips are often formed at high cutting speeds. Adiabatic shear bands, a form of failure mechanism and a precursor to ductile fracture occur in titanium alloys, are usually very narrow (5–500 μm) and they consist of highly sheared material. Adiabatic shear bands become apparent after 60 m/min cutting speed and usually above a feed of 0.05 mm/rev.

In room temperature, titanium has hexagonal close-packed (hcp) crystalline structure known as α-Ti but it forms body-centered cubic (bcc) crystalline structure at 827 °C (1100 K) known as β-Ti. This is often referred as *allotropic phase transformation* [12]. It is claimed that during machining process, due to low thermal conductivity of Ti–6Al–4V alloy, temperature may rise up rapidly to above allotropic phase transformation

* Corresponding author. Tel.: +1 732 445 1099; fax: +1 732 445 5467.
E-mail address: ozel@rutgers.edu (T. Özel).

0890-6955/$ - see front matter © 2010 Elsevier Ltd. All rights reserved.
doi:10.1016/j.ijmachtools.2010.08.004

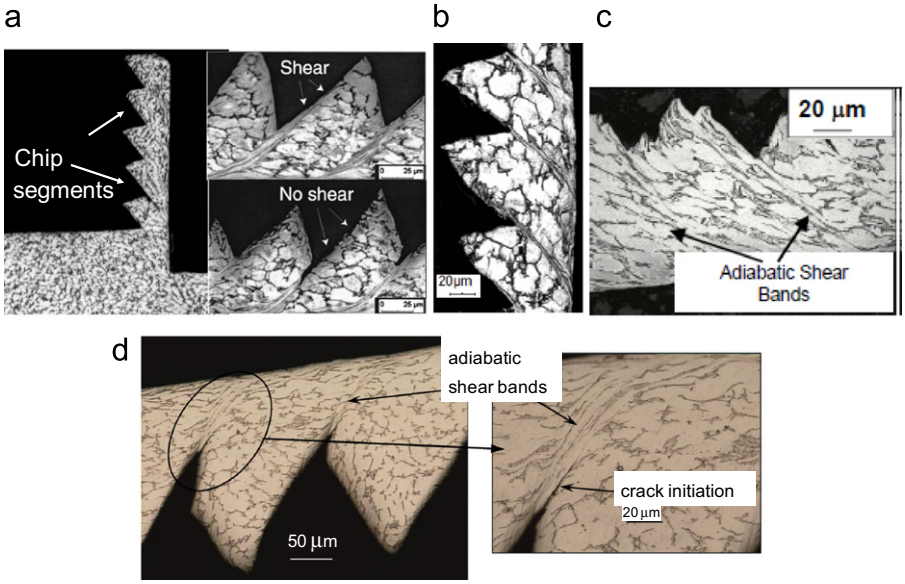

Fig. 1. Images of chip formation in orthogonal cutting of Ti–6Al–4V: (a) Baeker et al. [14]; (b) Gente and Hoffmeister [5], (c) Arrazola et al. [4], (d) Calamaz et al. [10].

temperature of this material (which is between 800 and 850 °C) and lattice structure of Ti–6Al–4V changes from hcp (α-phase) with fewer slip planes into bcc (β-phase) with more slip planes [12]. Increasing number of slip planes enables localized deformations and causes further instability and complexity in plastic deformation process with adiabatic shear bands resulting in formation of serrated chips [6–8]. Another conjecture claims that in addition to adiabatic shearing, there exists a crack initiation mechanism in the primary shearing zone (i.e. a narrow band between the tool tip and the chip free surface) which causes serration in the chips [5,13].

On the issue of *flow softening* and *dynamic recrystallization*, several studies are published. Miller et al. [15] reported that flow softening occurs during hot working of Ti–6Al–4V alloy especially temperatures near β-transus temperature (~900 °C) and at low effective strains (~0.05–0.5). Ding and Guo [16] investigated microstructural evolution of Ti–6Al–4V alloy during thermo-mechanical processing in the β-phase field and their experimental results indicated that flow softening due to dynamic recrystallization occurred during processing in the β-phase field. According to Cui et al. [17] dynamic recrystallization of α-phase occurs during hot deformation of Ti–6Al–7Nb alloy in the temperature range of 750–850 °C and the strain rates below 1 s^{-1}. At strain rates higher than 1 s^{-1} and temperatures above 800 °C, the material shows flow localization in β-phase. At β-transus temperature, the rapid increase of β-phase volume fraction entails that the deformation is controlled by dynamic recovery in β-phase. In a recent study Rittel et al. [18] observed nanometric grain sized shear bands and argues that in adiabatic shear bands Ti–6Al–4V alloy material experiences intense dynamic recrystallization posing a possible cause for shear failure during high rate deformation.

Finite element simulations have been developed to study the mechanics of machining, optimization of cutting conditions, and cutting tool design among other purposes. The ultimate goal is to eliminate expensive and time consuming experimental modeling approaches in favor of simulation models that are capable of producing realistic results at practical cutting conditions in process design.

In addition, they are commonly employed to simulate titanium machining because of their capability to model serrated chip formation. Often there are two group of approaches that are utilized to simulate serrated chip formation; (a) by using damage or material failure models [19–23] or (b) by using modified material models for temperature-dependent flow softening based adiabatic shearing [10,24,25].

In this paper, it is assumed that serration is caused by adiabatic shearing due to temperature-dependent flow softening therefore no damage or material failure model is considered. For this purpose, constitutive material models suggested for Ti–6Al–4V are investigated and a modified *temperature-dependent flow softening* model (i.e. Calamaz model [41]) is utilized. These models are employed in finite element simulations of 2D orthogonal cutting with plane strain analysis. The models are tested and verified by comparing experimental results to the finite element simulations outputs, mostly by comparing the chip morphology and cutting forces with the experimental data.

2. Material constitutive models

In finite element models, a constitutive material model is required to relate the flow stress to strain, strain rate and temperature. The experimental flow stress data are obtained by using the Split-Hopkinson pressure bar (SHPB) tests performed under various strain rates and temperatures. The experimental data obtained from these tests are used to calculate the unknown parameters of material constitutive models. Commonly used material models include: the Johnson–Cook (J–C) material model [26]; the Baummann–Chiesa–Johnson (BCJ) model [27]; the Maekawa model [28]; the micromechanical models [29,30]. Some of these models are discussed as they are pertinent to the temperature-dependent flow softening in Ti–6Al–4V alloy.

2.1. The Johnson–Cook material model

The Johnson–Cook (JC) material model [26] is widely used for analysis of material flow stress, especially for those materials which their flow stress is highly influenced by temperature and strain rate; the influence of strain, strain rate and temperature on the flow stress is defined by three multiplicative yet distinctive terms:

$$\sigma = (A + B\varepsilon^n)\left(1 + C\ln\frac{\dot{\varepsilon}}{\dot{\varepsilon}_0}\right)\left[1 - \left(\frac{T - T_r}{T_m - T_r}\right)^m\right] \quad (1)$$

Table 1
Constants of J–C model suggested for Ti–6Al–4V alloy.

Reference	A	B	C	n	m
Lee–Lin [31]	782.7	498.4	0.028	0.28	1.0
Lee–Lin [32]	724.7	683.1	0.035	0.47	1.0
Meyer–Kleponis [33]	862.5	331.2	0.012	0.34	0.8
Kay [34]	1098	1092	0.014	0.93	1.1
Seo et al. [35]	997.9	653.1	0.0198	0.45	0.7

where σ is the equivalent flow stress, ε is the equivalent plastic strain, $\dot{\varepsilon}$ is the equivalent plastic strain rate, $\dot{\varepsilon}_0$ is the reference equivalent plastic strain, T is the workpiece temperature, T_m is the material melting temperature and, T_r is the room temperature. However, based on the experimental works done by researchers different values for these constants were offered which are given in Table 1.

The J–C model constants shown in Table 1 are obtained at different testing conditions. Lee and Lin [31] obtained them at a constant strain rate of 2000 s^{-1} and a maximum true strain of 0.3 mm/mm, later they reported another set of parameters that were obtained at strain rates of 500–3000 s^{-1} and maximum strain as 0.35 with temperatures up to 1100 °C [32]. Meyer and Kleponis [33] used strain rate levels of 0.0001, 0.1 and 2150 s^{-1} and a maximum plastic strain of 0.57 mm/mm. Kay [34] tested Ti–6Al–4V alloy under strains up to 0.6 mm/mm and strain rates up to 10^4 s^{-1}. Seo et al. [35] tested the same material at temperatures up to 1000 °C and strain rates of 1400 s^{-1} and strains up to 0.25 mm/mm.

The J–C constitutive material model can be represented as a combination of three functions as

$$\sigma = f(\varepsilon)g(\dot{\varepsilon})h(T) \tag{2}$$

where

$$f(\varepsilon) = (A + B\varepsilon^n) \tag{3}$$

$$g(\dot{\varepsilon}) = \left(1 + C\ln\frac{\dot{\varepsilon}}{\dot{\varepsilon}_0}\right) \tag{4}$$

$$h(T) = \left[1 - \left(\frac{T - T_r}{T_m - T_r}\right)^m\right] \tag{5}$$

In this form, functions $f(\varepsilon)$, $g(\dot{\varepsilon})$, and $h(T)$ represent strain hardening, strain rate sensitivity and thermal softening behaviors of the work material, respectively. Often the SHPB test data fitted to those functions separately (one by one). Despite the abilities of this constitutive model to represent material behavior by taking into account of strain and strain rate hardening as well as thermal softening phenomenon; it still has some weak points as it can be summarized as follows: (a) the model is not applicable for all materials since some materials exhibit different behavior, (b) the model is meaningful in certain ranges of strain and strain rate but fails to capture high strain behavior e.g. flow softening, (c) fails to take into account the coupling effects of strain, strain rate and temperature e.g., $g(\varepsilon,\dot{\varepsilon})$ and $h(\varepsilon, T)$. Because of these known deficiencies, some of the researchers suggested modifications to the J–C constitutive model.

2.2. The Andrade–Meyers modified Johnson–Cook material model

Andrade and Meyers [36] suggested a modification term to the J–C model in order to describe the material response above recrystallization temperature in which, the flow stress is affected by phase transformations:

$$\sigma = f(\varepsilon)g(\dot{\varepsilon})h(T)H(T) \tag{6}$$

This modification term for the material flow stress behavior above the recrystallization/recovery temperature is

$$H(T) = \frac{1}{1 - [1 - ((\sigma_f)_{rec}/(\sigma_f)_{def})]u(T)} \tag{7}$$

where

$$\begin{cases} u(T) = 0 & \text{if } T < T_c \\ u(T) = 1 & \text{if } T > T_c \end{cases}$$

2.3. The Calamaz modified Johnson–Cook material model

Another modification to the J–C model is suggested by Calamaz et al. [10] for Finite Element simulations. These modifications included flow softening at elevated strains and temperatures. In the Calamaz model [41], flow softening is defined as a decreasing behavior in flow stress with increasing strain beyond a critical strain value. Nonetheless, below that critical strain, the material still exhibits strain hardening. The flow softening modifiers suggested to be included in the modified J–C flow stress model are as follows:

(a) modified strain hardening function of the original J–C model by including flow softening at higher strain values as

$$f(\varepsilon) = A + B\varepsilon^n\left(\frac{1}{\exp(\varepsilon^a)}\right) \tag{8}$$

(b) modified thermal softening function of the original J–C model by including temperature-dependent flow softening as

$$h(T) = \left[1 - \left(\frac{T - T_r}{T_m - T_r}\right)^m\right]\left[D + (1 - D)\tanh\left(\frac{1}{(\varepsilon + S)^c}\right)\right] \tag{9}$$

where $D = 1 - (T/T_m)^d$, and $S = (T/T_m)^b$.

Hence the Calamaz modified J–C material model developed by Calamaz [41] is given as

$$\sigma = \left(A + B\varepsilon^n\left(\frac{1}{\exp(\varepsilon^a)}\right)\right)\left(1 + C\ln\frac{\dot{\varepsilon}}{\dot{\varepsilon}_0}\right)\left[1 - \left(\frac{T - T_r}{T_m - T_r}\right)^m\right]\left(D + (1 - D)\tanh\left(\frac{1}{(\varepsilon + S)^c}\right)\right) \tag{10}$$

2.4. The Nemat-Nasser micromechanical model

Nemat-Nasser and co-workers have studied high strain rate dynamic material behavior of metals extensively [12,29]. They observed that at relatively high temperatures, flow stress, while monotonically decreasing as a function of temperature, exhibits sudden increase at a critical temperature and begins to decrease with further increase in temperature. This phenomenon is known as *dynamic strain-aging*. However, many constitutive models developed for Ti–6Al–4V alloy do not include the effect of dynamic strain aging. Moreover, Nemat-Nasser et al. [12] studied the dependence of the flow stress on the temperature and strain rate at different strains on workpieces which due to different ways of preparation had various microstructures, and the result was that this dependence is related to the material microstructure. Besides, based on the experiments they have found that adiabatic shear bands and the related fracture are developed at

high strain rates (any temperature) and at high temperatures (any strain rate). These shear bands are initiated once the magnitude of strain reaches to a certain level depending on the material temperature. Anurag and Guo [37] proposed a micromechanical constitutive model to predict the material behavior of Ti–6Al–4V titanium alloy based on the work of Nemat-Nasser and his co-workers [12,29]. In their model, the effect of strain rate and temperature on the flow stress is considered with a *thermally activated stress*, σ^*, term and the effect of microstructure (i.e. dislocation density, resistance of the lattice to dislocation motion, slip system, subgranular slip, or grain boundary glide) is represented with an *athermal stress*, σ_a, term as

$$\sigma = \sigma_a + \sigma^* \tag{11}$$

where $\sigma_a = \sigma_0 \varepsilon^n$ and

$$\sigma^* = g(T,\dot{\varepsilon}) = \hat{\sigma}\left\{1 - \left[-\frac{k}{G_0} T \left(\ln\frac{\dot{\varepsilon}}{\dot{\varepsilon}_0}\right)\right]^{1/q}\right\}^{1/p} \tag{12}$$

In thermally activated stress term, k is Boltzmann constant and G_0 is the total energy barrier, p and q are constants, $0 < p < 1$ and $1 < q < 2$.

It is found that specimen's microstructure only affects the athermal part of the flow stress, but not the thermally activated part which is dependent on temperature and strain rate [12]. Anurag and Guo [37] used the SHPB test results reported in Lee and Lin [32] and calculated the athermal part of the flow stress by considering the critical temperature at which flow stress becomes insensitive to temperature changes. They identified the critical temperature at which dynamic strain aging occurs from the stress vs. temperature plots obtained using the SHPB test results at a given strain rate. The athermal stress representation was obtained by a curve fitting approach from the strain vs. flow stress data at the identified critical temperature. The thermal stress below the critical temperature can be calculated by subtracting the athermal stress from the total stress at different strains. In order to predict flow stress above the critical temperature, they multiplied the athermal stress with a temperature coefficient and obtained a good fit to experimental flow stress data.

In summary, the effects of strain hardening, thermal softening, dynamic strain aging, etc. are considered in these models. The levels of strain and strain rate observed at shear zones during machining are much higher than those attained by using the SHPB tests. As a result, the flow stress at high strains beyond the experimental range is calculated by extrapolation using constitutive models. The need to modify these material models is related to the material behavior at strains higher than strain ranges achievable with the Split-Hopkinson Pressure Bar tests. In machining, the strains are much higher in the deformation zones ($\varepsilon > 1$).

3. Dynamic material behavior of titanium alloy

In room temperature, titanium (an allotropic element) has hcp crystalline structure known as α-Ti but forms bcc crystalline structure around 900 °C known as β-Ti. Aluminum and vanadium are used as phase stabilizers to obtain $\alpha+\beta$ alloy phase [29]. As given in Table 1, dynamic material behavior data for Ti–6Al–4V titanium alloy have been widely published in literature [31–35]. Lee and Lin [32] investigated temperature and strain-rate sensitivity of Ti–6Al–4V alloy and presented some SHPB test results at temperatures from 20 to 1100 °C, with strain rates from 800 up to 3300 s^{-1} as shown in Fig. 2.

Several years later, Nemat-Nasser et al. [12] have studied the dynamic behavior of Ti–6Al–4V alloy with different microstructures using the SHPB compression tests at strain rates ranging from 1000 to 7000 s^{-1}, and initial temperatures ranging from 77 up to 1000 K. The dependence of the flow stress on the temperature and the strain rate at various strains was related to the material microstructure. Their results indicated that adiabatic shear bands develop at high strain rates as well as at low strain rates and high temperatures and flow stress is more sensitive to temperature than to the strain rate. They claimed that *thermally activated dislocation motion mechanisms* are responsible for *adiabatic shear bands*. One of the revealing results of that study was the flow softening behavior of the flow stress curve at strain rate of 1 s^{-1} and temperature of 980 °C above the strain value of 0.3. Since there was no flow stress data presented below 960 °C, it was not possible to discuss possible dynamic strain aging behavior of Ti–6Al–4V. In summary, it was concluded that flow stress of Ti–6Al–4V alloy is more sensitive to the temperature than to the strain rate [12].

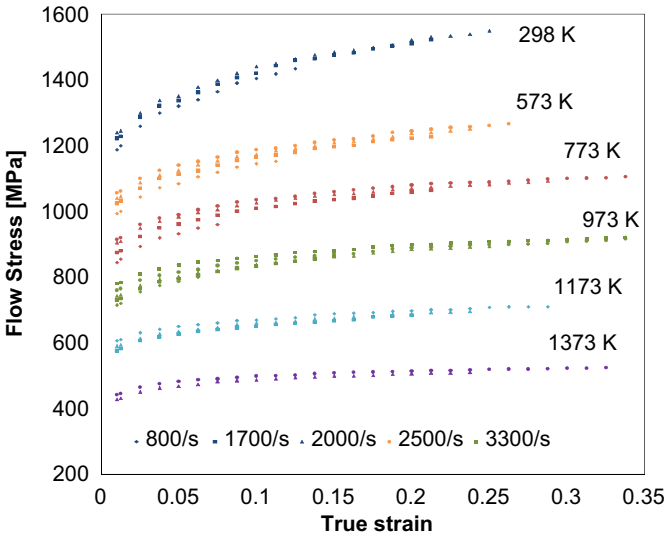

Fig. 2. Flow stress data obtained from SHPB tests by Lee and Lin [2].

3.1. Adiabatic shearing and flow softening phenomenon

In machining titanium alloys, it is commonly known that plastic instability and adiabatic shearing related chip serration occurs. Work material often goes to secondary shearing after primary shearing zone and saw-tooth shape regular chip segments form. The underlying cause of chip serration is often associated with adiabatic shearing [8]. Recent studies have considered the effects of flow softening and adiabatic shearing effect on the behavior of titanium Ti–6Al–4V alloy at high strains [10,38]. The flow softening is believed to be related to dynamic recovery and/or recrystallization occurring after a critical value of strain. The effect of flow softening is more pronounced at low temperatures, and as temperatures increase, both strain hardening and flow softening effects are reduced. Recently, Calamaz et al. [10] modified the J–C material constitutive model by multiplying it with a function in order to include flow softening in their simulations. They were able to simulate serrated chip formation resembling experimental chips. They did not study the influence of different flow softening parameters on the simulations. Sun and Guo [38] pointed out the difference between machining and compression tests and considered the adiabatic effect on the flow stress. They calculated shear flow stress during machining by using an orthogonal machining model and showed

that flow stress values obtained at high strains are much lower than flow stress values obtained under isothermal conditions with compression tests. In this study, the strain-rate and temperature sensitivity as well as interrelationship between strain–strain rate and softening at high strains in dynamic behavior of Ti–6Al–4V alloy is also investigated.

3.2. Strain-rate and temperature sensitivity

The influence of increasing strain rate on the flow stress is represented with strain rate sensitivity parameter β, defined as

$$\beta = \frac{(\sigma_2 - \sigma_1)}{\ln(\dot{\varepsilon}_2/\dot{\varepsilon}_1)} \tag{13}$$

Strain rate sensitivity is calculated by considering the difference in flow stress values at two different strain rate levels at each strain using Eq. (13) and it is found that strain rate sensitivity decreases with increasing strain [32]. The influence of increasing temperature on the flow stress, i.e. temperature sensitivity, is represented with a parameter n_a defined as

$$n_a = \frac{\{\ln(\sigma_2/\sigma_1)\}}{\{\ln(T_2/T_1)\}} \tag{14}$$

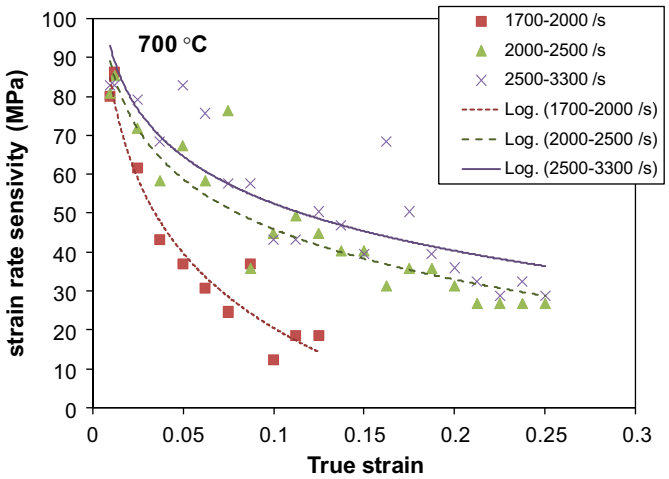

Fig. 3. The relationship between strain rate sensitivity and true strain (at 700 °C).

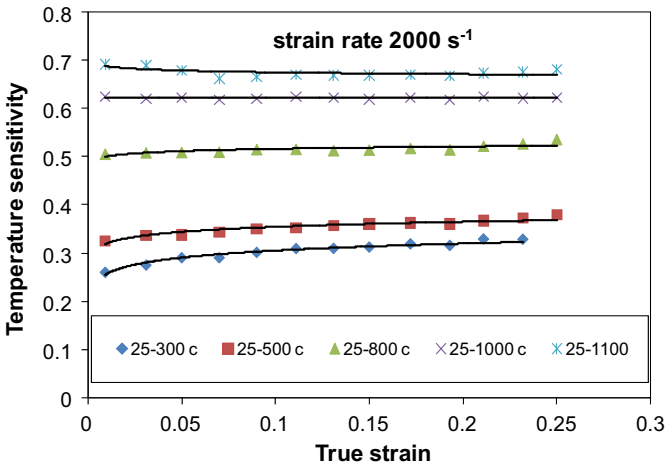

Fig. 4. The relationship between temperature sensitivity and true strain.

where $T_2 > T_1$, and $T_1 = 25$ °C. Using Eq. (14), temperature sensitivity is calculated similarly. The resultant strain rate sensitivity and temperature sensitivity are shown in Figs. 3 and 4 by using the flow stress data given in Fig. 1. During deformation, the rate of thermal softening caused by increasing temperatures is found greater than that of strain hardening induced by plastic deformation, and thus it can be seen that strain rate sensitivity decreases rapidly with increasing strain for all the strain rate ranges.

4. Modified material constitutive models

As discussed earlier, localized flow softening phenomenon can be described as offering less resistance to local plastic deformations due to rearrangement of dislocations caused by subsequent cycling or dynamic recrystallization in the material. This phenomenon is usually observed during an increase in strain beyond a critical strain value together with a rapid rise in material's temperature. Flow softening is believed to cause adiabatic shearing within the primary shear zone. Thus, chip segmentation with shear bands are formed as the deformed material leaves this zone.

For this reason, modified material constitutive models with flow softening resulting from strain softening and temperature softening are sought in literature. By developing such a modified constitutive model and implementing it into Finite Element software Forge-2D, Calamaz et al. [10] were able to simulate serrated chip formation in machining of titanium alloy Ti–6Al–4V.

4.1. Modified material model with non-temperature-dependent parameters (Model 1)

During flow softening, flow stress begins to decrease with increasing strain beyond a critical strain value and resumes strain hardening behavior with further increase in strain. Below that critical strain, the material exhibits strain hardening. Therefore, a flow softening modification should be included in the modified J–C constitutive material model.

In order to include the effect of flow softening at high strains, another term is integrated into flow stress as shown in Eq. (15). The purpose of using *tanh* function is to leave flow stress at low (experimental) strains unchanged and introduce different levels of softening at higher strains through parameters p, r, S, and M:

$$g(\varepsilon) = M + (1-M)\left[\tanh\left(\frac{1}{(\varepsilon+p)^r}\right)\right]^s \tag{15}$$

Thus, this modified J–C model with an overarching flow softening modifier becomes

$$\sigma = (A + B\varepsilon^n)\left(1 + C\ln\frac{\dot{\varepsilon}}{\dot{\varepsilon}_0}\right)\left[1 - \left(\frac{T-T_r}{T_m-T_r}\right)^m\right]\left[M + (1-M)\left[\tanh\left(\frac{1}{(\varepsilon+p)^r}\right)\right]^s\right] \tag{16}$$

In this modified J–C material model, the SHPB test data obtained at high strain rates and high temperatures by Lee and Lin [32] as given in Fig. 2 is employed.

Hence, a modified J–C model (*Model 1*) using an overarching modifier that includes flow softening effect can be introduced. The flow stress curves depicting flow softening effect in *Model 1* are presented in Fig. 5. The parameter M substantially modifies the flow stress after a critical value of strain (ε_c) around 0.5 mm/mm. However, it should be noted that flow softening is equally applied to flow stress at all temperatures.

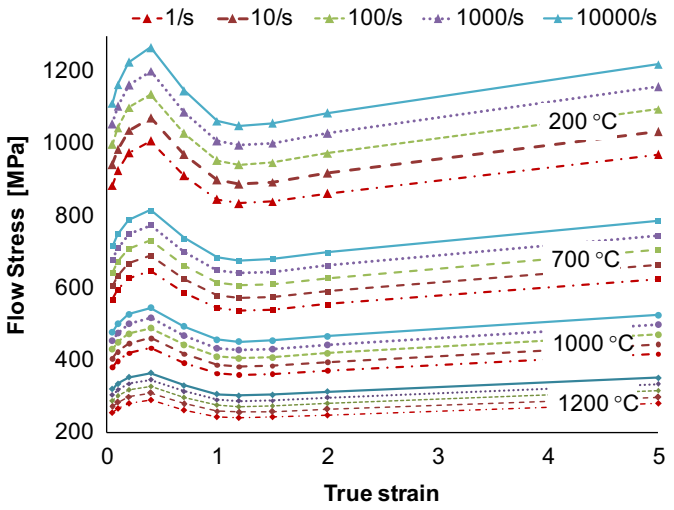

Fig. 5. Flow stress curves using modified material model, *Model 1* ($M=0.7$, $S=7$, $p=0$, $r=1$).

4.2. Modified material model with temperature-dependent parameters (Model 2)

Modifications to the thermal softening part of the J–C model by including *temperature-dependent flow softening* parameters are proposed and the model is given in

$$\sigma=\left[A+B\varepsilon^{n}\right]\left[1+C\ln\frac{\dot{\varepsilon}}{\dot{\varepsilon}_0}\right]\left[1-\left(\frac{T-T_r}{T_m-T_r}\right)^{m}\right]\left[D+(1-D)\left[\tanh\left(\frac{1}{(\varepsilon+p)^{r}}\right)\right]^{s}\right] \tag{17}$$

where in this model, the parameters D and p are dependent on the workpiece temperature, T, as following:

$$D=1-\left(\frac{T}{T_m}\right)^{d} \quad \text{and} \quad p=\left(\frac{T}{T_m}\right)^{b}$$

Temperature dependency of the overarching modifier is governed by the exponents d and b which enhances the softening behavior of the flow stress at elevated temperatures (see Fig. 6), since this phenomenon may be related to phase transformation and recrystallization of the material which may occur at a certain temperature range. This dependency on temperature and its effect on the flow stress model appears more reasonable than *Model 1* as shown in Fig. 6. Flow softening gradually occurs with increasing temperature.

4.3. Modified material model with temperature-dependent parameters and strain softening (Model 3)

Further modifications to the strain hardening part of the J–C model by including flow softening at higher strain values are proposed and the model is given in Eq. (18). This model is almost identical to the Calamaz modified J–C material model. Here an exponent S is introduced to further control *tanh* function for thermal softening.

$$\sigma=\left[A+B\varepsilon^{n}\left(\frac{1}{\exp(\varepsilon^{a})}\right)\right]\left[1+C\ln\frac{\dot{\varepsilon}}{\dot{\varepsilon}_0}\right]\left[1-\left(\frac{T-T_r}{T_m-T_r}\right)^{m}\right]\left[D+(1-D)\left[\tanh\left(\frac{1}{(\varepsilon+p)^{r}}\right)\right]^{s}\right] \tag{18}$$

where $D=1-(T/T_m)^{d}$ and $p=(T/T_m)^{b}$.

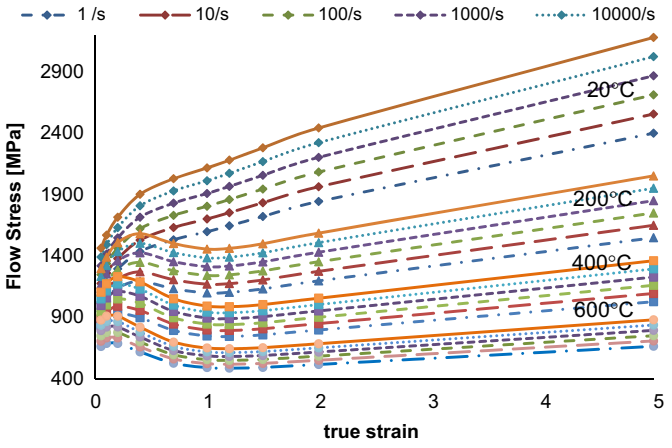

Fig. 6. Flow stress curves using modified material model, *Model 2* ($r=1$, $d=0.5$, $b=1$, $S=5$).

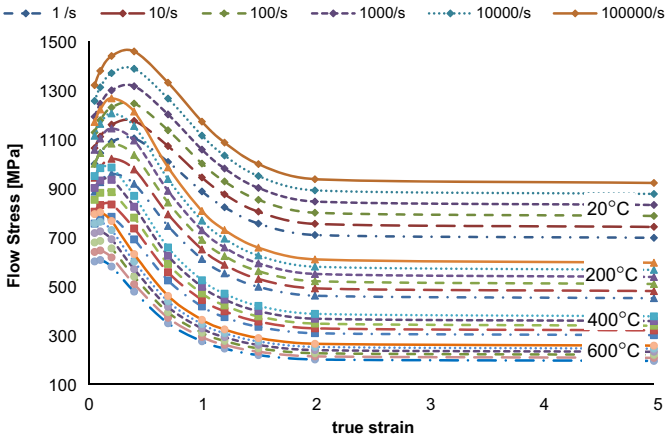

Fig. 7. Flow stress curves using modified material model, *Model 3* ($a=2$, $r=1$, $d=0.5$, $b=1$, $S=5$).

Again, the experimental flow stress curves obtained by Lee and Lin [32] have been taken as the base for this Calamaz modified J–C model. In this modified model (*Model 3*), a multiplicative term is added to the strain hardening part, causes dependency of flow softening phenomenon not only upon temperature, but also on strain, as it can been seen in Fig. 7. This additional term affects the softening behavior of flow stress at a controlled range of strain.

In order to identify the model parameters in *Model 3*, the effects of parameters, a, b, d, r and S on the flow stress curves at high strain ranges and high temperatures are studied, while maintaining a good agreement between the model generated flow stress curves and the SHPB test data obtained from Lee and Lin [32].

In order to study the effects of the parameters used in the flow softening terms (either the ones added to thermal softening part or strain hardening part), one parameter is varied while other parameters are held constant.

In Figs. 8–11, SHPB experimental data obtained by Lee and Lin [32] in the range of strains below 0.3 mm/mm which was the limitation of the apparatus, and the flow stress curves generated by the model (dotted lines) are compared for a range of model parameters at temperatures of 300, 500 and 700 °C. While proposed material flow stress model is compared with experimental data at lower strains, its behavior at higher strain ranges which are typical in cutting process (0.5 mm/mm $<\varepsilon<5$ mm/mm) is investigated. The best fitting parameters are

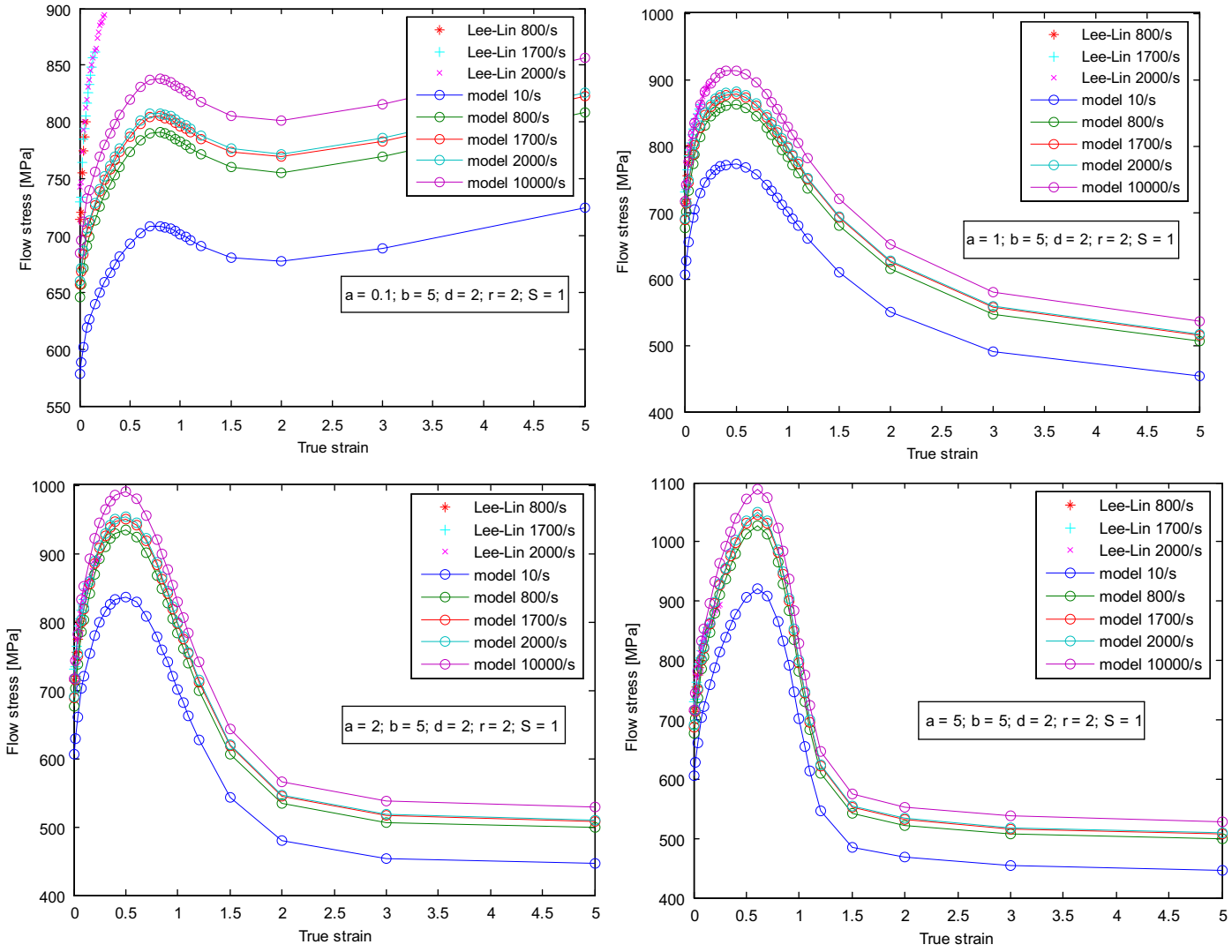

Fig. 8. Flow stress curves depicting the effects of parameter *a* at 700 °C.

identified by using a factor screening method that resulted in good agreement of the model generated flow stress curves with the SHPB test data. In factor screening, a wide range of values for each factor (model parameter) is initially utilized and the ranges of each factor significantly affecting the flow softening behavior are identified. This method is repeated until a suitable parameter range is obtained.

As shown in Fig. 8, parameter *a* controls the strain hardening part by decreasing flow stress after a critical strain value (ε_c). It should be noted that a low value of parameter *a* results in a mismatch to the SHPB test data. Increasing the parameter *a* from a value of 1–5 creates a sharper decline in flow stress curve and a larger drop at higher strain regions. The parameter *b* in the *tanh* function (see Eq. 18) controls the temperature-dependent flow softening effect and where (i.e. in which strain) peak or maximum flow stress would take place. The lower the value of parameter *b*, the lower the strain value of the peak flow stress occurs. A higher value of parameter *b* also increases the value of the peak flow stress as shown in Fig. 9.

The parameter *d* which is an exponent for the temperature controls the degree of temperature dependency of parameter *D* as given in Eq. (18). The parameter *d* has a strong impact on the value of flow softening and determines the minimum flow stress value as shown in Fig. 10. It does not affect the corresponding strain value for peak flow stress.

The parameter *S*, which controls the *tanh* function in thermal softening at elevated strains and temperatures together with parameters *b*, *d* and *r*, also controls the softening trend. A higher value of the parameter *S* leads to a faster entrance to the softening regime with respect to increasing strain and decreases the slope of the softening part of the flow stress curves without changing the value of the minimum flow stress as shown in Fig. 11. A lower value of the parameter *S* causes minimum flow stress to take place at a higher strain. Parameters *r* and *S* have interacting but similar effects on the flow stress.

5. Orthogonal machining of titanium alloy Ti–6Al–4V

Orthogonal turning of Ti–6Al–4V titanium alloy tubes (50.8 mm diameter and 3.175 mm thick) have been performed using uncoated tungsten carbide (WC/Co) cutting tools in a rigid CNC turning center at TechSolve Inc., Cincinnati, Ohio. The cutting forces were measured with a force dynamometer and high-speed data acquisition devices. The experiments have been conducted using uncoated carbide tools (WC/Co) with sharp edges (around

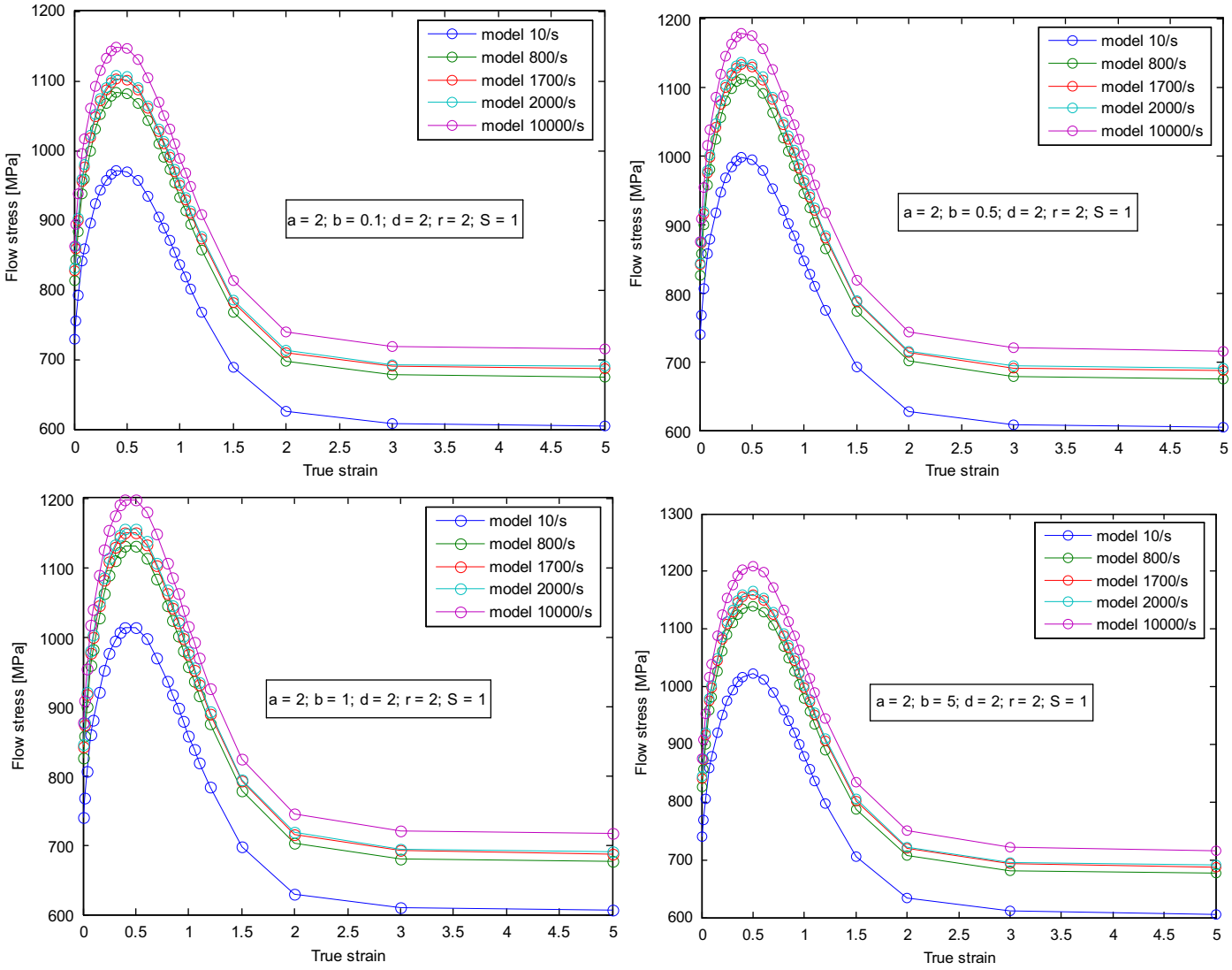

Fig. 9. Flow stress curves depicting the effects of parameter b at 500 °C.

5 μm edge radius) and TiAlN coated carbide (WC/Co) using a tool holder that provided $\gamma=0^\circ$ and 5° rake (effective) angle and 11° and 6° relief angle respectively at two different cutting speeds ($v_c=121.9$, 240.8 m/min) and five different feeds (or uncut chip thickness) ($t_u=0.0254$, 0.0508, 0.0762, 0.1016, 0.127 mm/rev). Cutting forces measured in orthogonal turning tests of Ti–6Al–4V titanium alloy tubes have been presented in Fig. 12. All experiments are performed at dry orthogonal turning conditions and replicated at least twice at each condition.

The cutting forces were generally lower at the positive rake angle ($\gamma=5^\circ$) and at the lower cutting speed ($v_c=121.9$ m/min). The thrust forces were much lower when using a positive rake angle ($\gamma=5^\circ$) tool holder with TiAlN coated carbide inserts at the higher cutting speed ($v_c=240.8$ m/min).

There was a significant increase in thrust force with an increase in cutting speed however this increase becomes small at increased feeds (>0.076 mm/rev) and at the lower cutting speed.

It is reported in literature that the relationship between thrust force and cutting speed in machining Ti–6Al–4V is mainly affected by the interfacial conditions at the tool rake face. As the temperatures increase titanium alloy tends to weld itself to the rake face and creates higher thrust forces [4,9].

However, at the same cutting conditions, TiAlN coated carbide tools resulted always higher cutting and thrust forces. It is believed that the effect of larger edge radius (r_β) due to added layer of coating (TiAlN) becomes the dominant mechanism on increased forces.

The larger edge radius in coated tools hinders their potential benefits in tool life, hence results in significantly higher forces especially when cutting speed is increased from $v_c=121.9$ m/min to $v_c=240.8$ m/min. Hence, it may be beneficial to modify edge preparation of the coated tools (TiAlN) to lower the effects of increasing cutting edge radius.

In order to take measurements on the chip cross-sections, chips were embedded into black-epoxy, polished and etched. The images of micro-chip geometries were captured with optical digital microscopy at Rutgers University facilities. In Fig. 13, serrated chips obtained under different cutting conditions are shown.

It is observed that degree of serration increase with increasing feed or uncut chip thickness and increasing cutting speed. There were no significant effects of rake angle and tool coating on the degree of serration.

The chips produced at lower cutting speeds and feeds as shown in Fig. 13 are fairly uniform along their thickness with less

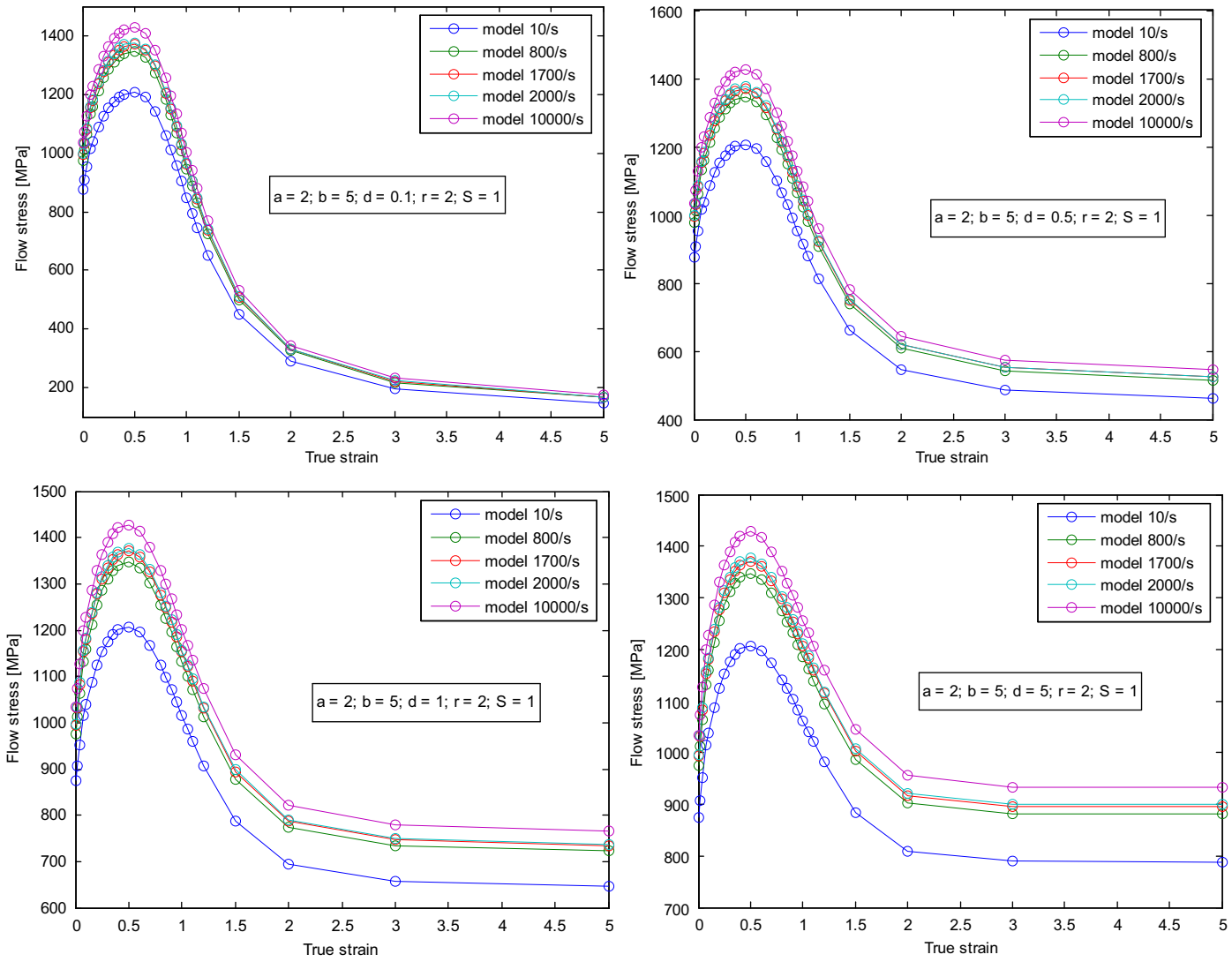

Fig. 10. Flow stress curves depicting the effects of parameter d at 300 °C.

similar to "saw-tooth" shapes. Whereas, the chips at high feeds at both cutting speeds show a clear periodic "saw-tooth" shape formation with mostly uniform size segments after a single large segment and then same pattern is repeated.

6. Finite element simulations

In this study, finite element (FE) simulations are developed using updated Lagrangian software (DEFORM-2D) in which chip separation from workpiece is achieved with continuous remeshing. Throughout this study, only coupled *thermo elasto-viscoplastic* finite element simulations are considered. These elasto-viscoplastic simulations included a workpiece as elasto-viscoplastic with a mesh containing 10,000 quadrilateral elements with element size ranging from 2 to 60 μm. Tool is modeled as rigid with a mesh containing into 2500 elements. A high density mesh in the primary deformation zone was applied as shown in Fig. 14. A sensitivity analysis is conducted so that the number of elements in the mesh is large enough and the workpiece mesh does not influence the predictions obtained with the FE simulations. A tool edge radius of r_β=5 μm for uncoated carbide (WC/Co) and r_β=10 μm for TiAlN coated carbide (WC/Co) are employed in the tool geometry. A thin layer of coating (5 μm thickness) is applied and meshed with elements ranging from 2 to 4 μm in size by using "coating" feature provided in the FE software. These simulation models are compared with experimental results obtained in this study.

A plane-strain coupled thermo-mechanical analysis was performed using orthogonal cutting assumption. Thermal boundary conditions are defined accordingly in order to allow heat transfer from workpiece to cutting tool. The heat conduction coefficient (h) is taken as 1000 kW m^{-2} K^{-1} to allow rapid temperature rise in the tool. Mechanical and thermo-physical properties of titanium Ti–6Al–4V alloy are defined as temperature dependent. Temperature-dependent (T in °C) Young's modulus (E), thermal expansion (α), thermal conductivity (λ), heat capacity (c_p) are given for Ti–6Al–4V alloy, and tool material and coating in Table 2.

6.1. Chip–tool interfacial friction model

The friction in machining is indeed complex and requires use of variable friction along the edge radius and rake face of the

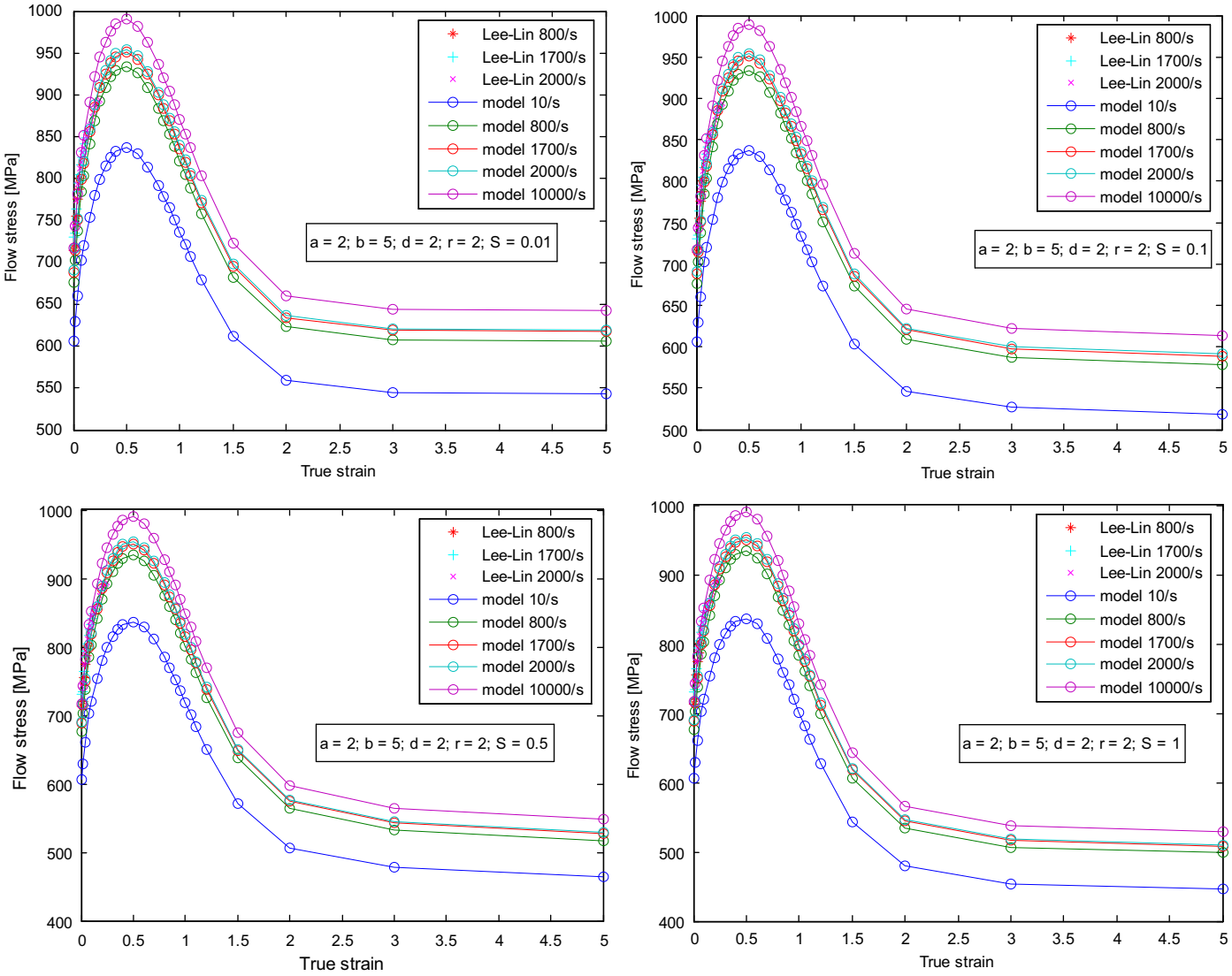

Fig. 11. Flow stress curves depicting the effects of parameter S at 700 °C.

insert [39]. Friction factor, which is defined as $m=\tau/k$ where τ is frictional shear stress and k is the work material shear flow stress, is commonly used at severe contact conditions whereas a Coulomb friction coefficient is applied to mild contact conditions. Friction along the tool rake face when curvilinear edge inserts are employed is more sophisticated. At the rake face, friction factor decreases with increasing ratio of uncut chip thickness, t_u, to edge radius, r_β, and increasing cutting speed [40].

In this paper similar to the previous work by the authors [24,25], three contact and friction regions are considered at the tool–chip interface: (i) a sticking region from the tool tip point to the end of the round edge curvature ($\tau=k$ or $m=1$), (ii) a shear friction region ($m=0.85$ for uncoated WC/Co and $m=0.9$ for TiAlN coated WC/Co) from the end of the curvature to the uncut chip thickness boundary, (iii) a sliding region along the rest of the rake face (a friction coefficient $\mu=0.5$) as shown in Fig. 15.

6.2. Simulation experiments for model validation

In these simulations, serrated chip formation process is simulated from the incipient to the steady-state by using adiabatic shearing based on flow softening elasto-viscoplastic work material assumption. A set of simulations for benchmarking the modified J–C models (*Model 1*, *Model 2* and *Model 3*) is conducted. Several modified model parameters have been tested against each other at the same cutting condition (uncoated WC/Co tool, $v_c=121.9$ m/min, $t_u=0.1$ mm/rev, $\gamma=0^\circ$, $r_\beta=5$ μm). The resultant force and chip geometry predictions (average minimum segmented chip thickness, t_{c_min}, average maximum segmented chip thickness t_{c_max} and pitch between two chip segment crests, p, are compared with experimental ones as shown in Table 3.

For example, the influence of modified J–C model (*Model 1*) parameters on the serrated chip formation can be seen in Fig. 16. After several iterations, the model parameters highlighted in Table 3 are chosen as the most suitable parameters to modify J–C material model without changing the Lee and Lin [32] SHPB test data which are mostly obtained at lower strains.

In order to compare modified material models for force predictions, force generations in FE simulations with respect to cutting time are also compared with the experimentally measured cutting (F_c) and thrust (F_t) forces as shown in Figs. 17 and

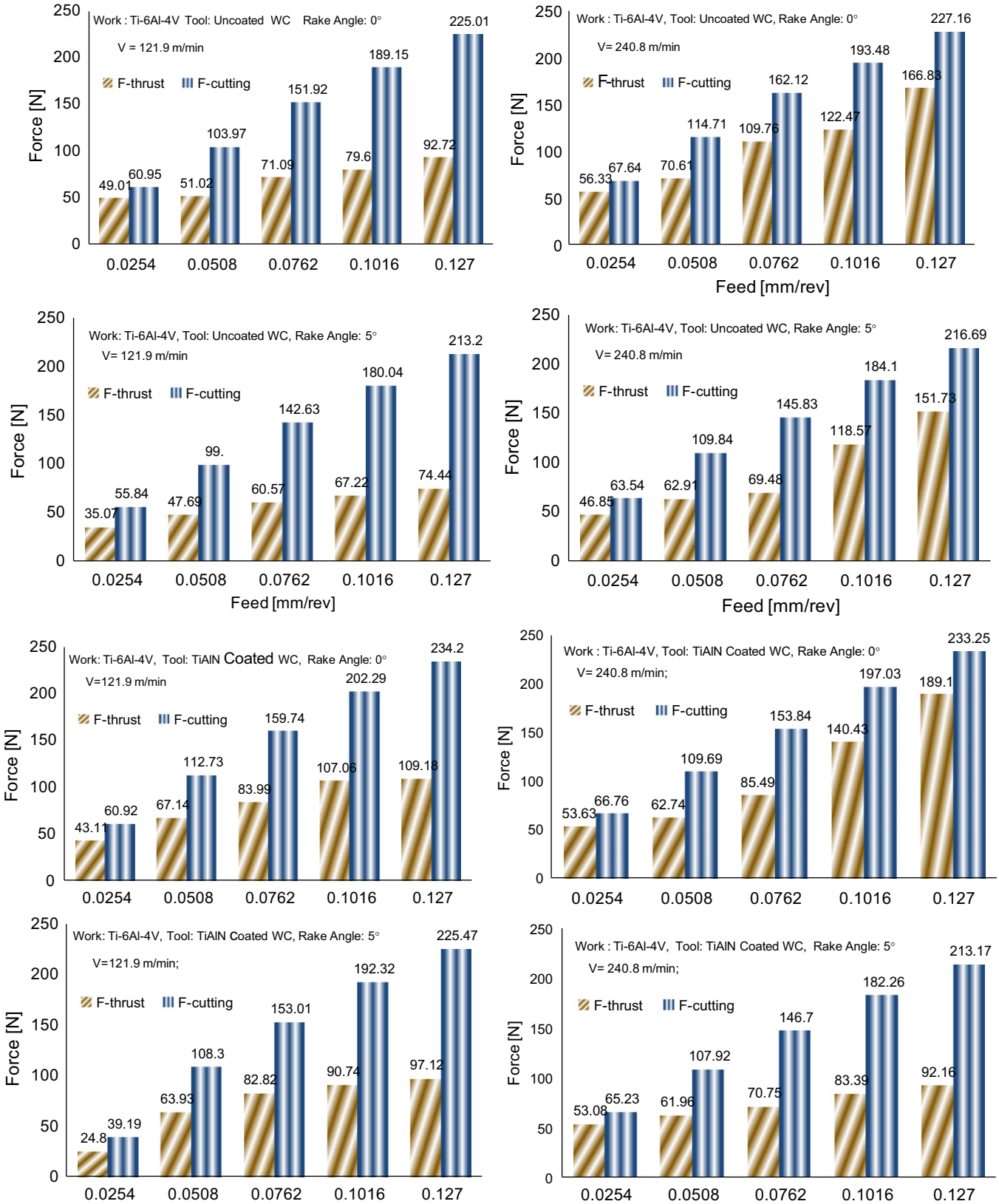

Fig. 12. Cutting and thrust forces in orthogonal cutting test of Ti–6Al–4V alloy.

18. Predictions obtained with simulations using *Model 3* have resulted in the closest matches to the experimental forces. This modified material model has also resulted in close agreement in cutting and thrust forces for the two other uncut chip thickness conditions as shown in Fig. 18. The force predictions can further be improved by adjusting the friction parameters implemented in

Fig. 13. Images of serrated chips at different cutting conditions.

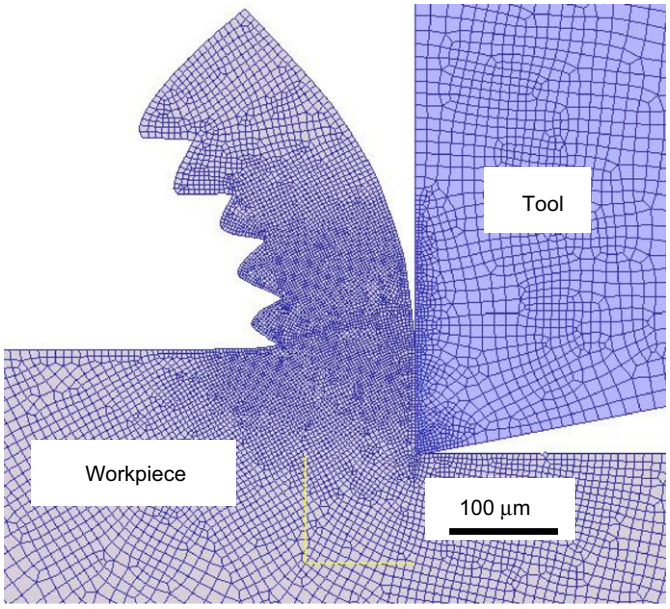

Fig. 14. Mesh for the workpiece and the tool.

variable friction definition with three distinct regions (sticking and slipping).

The effective strain distributions that are given in Fig. 19 show the adiabatic shear bands very clearly. In these simulations no damage criterion was used at all. Fig. 19 also shows the chip morphology for three different uncut chip thickness (t_u=0.075, 0.100, and 0.125 mm) using *Model 3* and comparison against *Model 1* and *Model 2* predictions. As it can be seen from the predicted serrated chips with finite element simulations, a large chip segment (tooth) is followed by a smaller one in almost all models similar to the observations reported by Calamaz et al. [10]. However, the difference is more visible in elasto-viscoplastic simulations using *Model 3* in Fig. 19.

Therefore, the temperature-dependent flow softening modified J–C material model (*Model 3*) which is very similar to the Calamaz modified material model is adapted as the flow stress for the simulation of machining Ti–6Al–4V alloy. Thus experimental data reported in this study have been used to validate the elasto-viscoplastic finite element simulations. Since influence of friction conditions on the simulation results is not the focus of this study, same friction parameters given have been applied to simulations with different modified J–C models.

Table 2
Mechanical and thermo-physical properties of work and tool materials used in FE simulations.

Property	Ti–6Al–4V titanium alloy	WC/Co tungsten carbide	TiAlN coating
E (T °C) [MPa]	$0.7412*T+113{,}375$	$5.6e^{5}$	$6.0e^{5}$
α (T °C) [mm mm^{-1} °C^{-1}]	$3.10^{-9}*T+7.10^{-6}$	$4.7e^{-6}$	$9.4e^{-6}$
$\lambda(T$ °C) [W m^{-1} °C^{-1}]	$7.039e^{0.0011*T}$	55	$0.0081*T$ + 11.95
$c_p(T$ °C) [N mm^{-2} °C^{-1}]	$2.24e^{0.0007*T}$	$0.0005*T+2.07$	$0.0003*T+0.57$

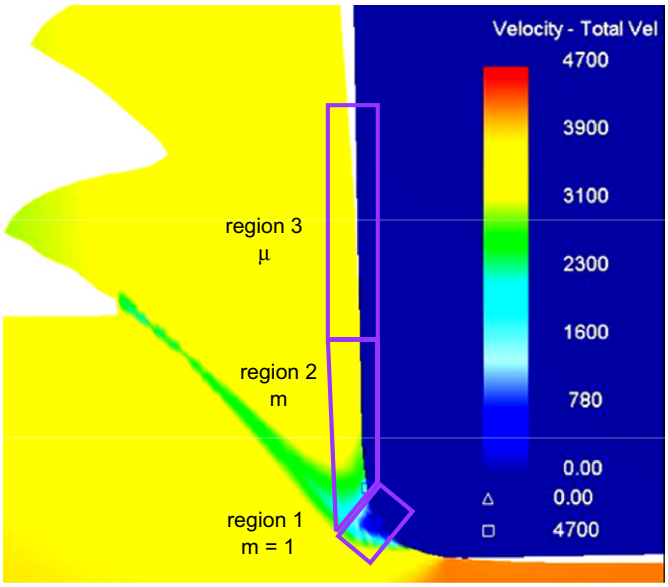

Fig. 15. Velocity field and friction regions defined in FE models.

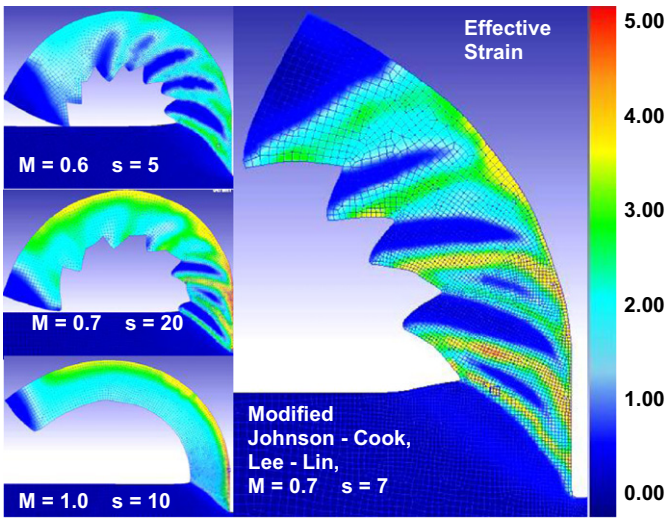

Fig. 16. Serrated chip formation with adiabatic shearing using *Model 1* (uncoated WC/Co tool, v_c=121.9 m/min, t_u=0.1 mm/rev, 0° rake angle, r_β=5 μm).

Adiabatic shear bands are clearly visible in the chips modeled by FE simulations by noting the values of the effective strain at the regions where a new segment starts to form; strain values at those areas are higher than other regions. Effective (equivalent) strain and stress values at 80 nodes along the path from P1 to P80 are plotted to investigate the flow softening in adiabatic shearing. In Fig. 20 by using temperature dependent flow softening material model *Model 3*, strain path obtained from FE simulation outputs exhibit increasing strain in the adiabatic shear bands and decreasing within the chip segments.

Effective stress along the same path is also plotted as shown in Fig. 21. Flow softening (lower effective stress) of the material leaving the primary shear zone and forming a chip segment is also observed in this plot. It should be noted that effective stress remains low within the chip segments due to high temperatures.

6.3. Simulation results

After selecting the *Model 3* with best fit parameters (S=0.05, a=2, r=1, d=1, b=5) for the specific cutting condition (v_c=120 m/min, t_u=0.1 mm/rev, 0° rake angle, r_β=5 mm), other cutting conditions also have been simulated by using this model. All FE simulations are run for 0.1 s cutting time. Predicted forces from simulations are compared with measured forces in orthogonal cutting tests of Ti–6Al–4V alloy tubes as shown in Fig. 22. Especially, cutting forces are in close agreements with 5% prediction error. Thrust force predictions which show 10–15% prediction error can be further improved with finer adjustments of friction regions and their values.

In Table 4, a comparison of simulated minimum and maximum serrated chip thickness and serration pitch with measurements is given. In addition, detailed comparisons of simulated effective strain distributions of the serrated chips with captures chip images are shown in Fig. 23 in which close agreements are observed.

In Fig. 24, temperature distributions for various cutting conditions are given. The maximum temperatures are also indicated in each distribution. The temperatures predicted are usually higher with uncoated WC/Co tools. Temperatures increase as undeformed chip thickness increases, or cutting speed increases and decreases as rake angle decreases.

7. Conclusions

In this study, influence of material constitutive models and elastic-viscoplastic finite element formulation on serrated chip formation for modeling of machining Ti–6Al–4V titanium alloy is investigated. Temperature-dependent flow softening based modified material models are considered where flow softening phenomenon, strain hardening and thermal softening effects and their interactions are coupled. Orthogonal cutting experiments have been conducted with uncoated carbide (WC/Co) and TiAlN coated carbide cutting tools. Temperature-dependent flow softening parameters are validated on a set of experimental data using measured cutting forces and chip morphology. Finite Element simulations are validated with experimental results at

Table 3
Benchmark FE simulations to identify modified material model parameters.

Experimental Simulation	F_{c_exp}=189 N/mm *ave.* F_c (range)	F_{t_exp}=90 N/mm *ave.* F_t (range)	t_{c_min}=0.13 mm t_{c_min} (mm)	t_{c_max}=0.192 mm t_{c_min} (mm)	p_{exp}=0.08 mm p (mm)
Model 1					
M=0.7, S=4, p=0, r=1	144 (120–160)	55 [37–66]	0.107	0.155	0.06
M=0.6, S=5, p=0, r=1	152 [110–185]	41 [57–26]	0.106	0.130	0.04
M=0.7, S=20, p=0, r=1	165 [140–190]	52 [42–65]	0.106	0.146	0.08
M=0.7, S=7, p=0, r=1	177 [154–196]	54 [45–64]	0.12	0.135	0.04
Model 2					
S=5, r=1, d=1, b=1	168 [138–187]	51 [40–70]	0.11	0.139	0.065
S=1.5, r=5, d=0.5, b=2	172 [120–200]	47 [26–64]	0.118	0.15	0.04
S=1.5, r=2, d=1, b=2	181 [148–194]	52 [44–75]	0.127	0.14	0.03
Model 3					
a=2.5, S=0.01, r=1, d=1, b=2	200 [170–240]	60 [50–70]	0.103	0.14	0.05
a=2.5, S=0.5, r=0.1, d=1,b=5	195 [163–216]	51 [41–69]	0.1	0.125	0.07
a=2, S=0.05, r=2, d=1, b=5	195 [175–230]	62 [50–72]	0.108	0.135	0.055

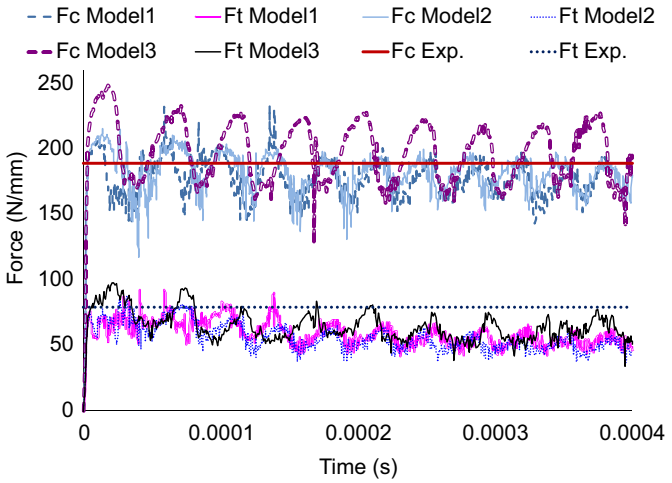

Fig. 17. Comparison of forces predicted (v_c =120 m/min, t_u=0.1 mm/rev, γ=0°, r_β=5 mm).

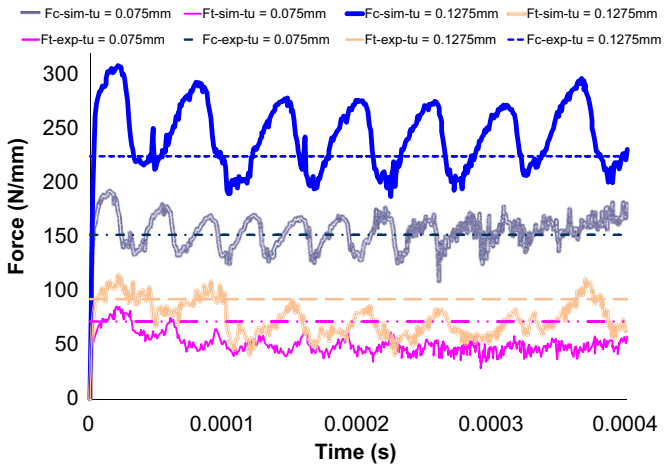

Fig. 18. Comparison of forces predicted with *Model 3* (v_c =120 m/min, γ=0°, r_β=5 μm).

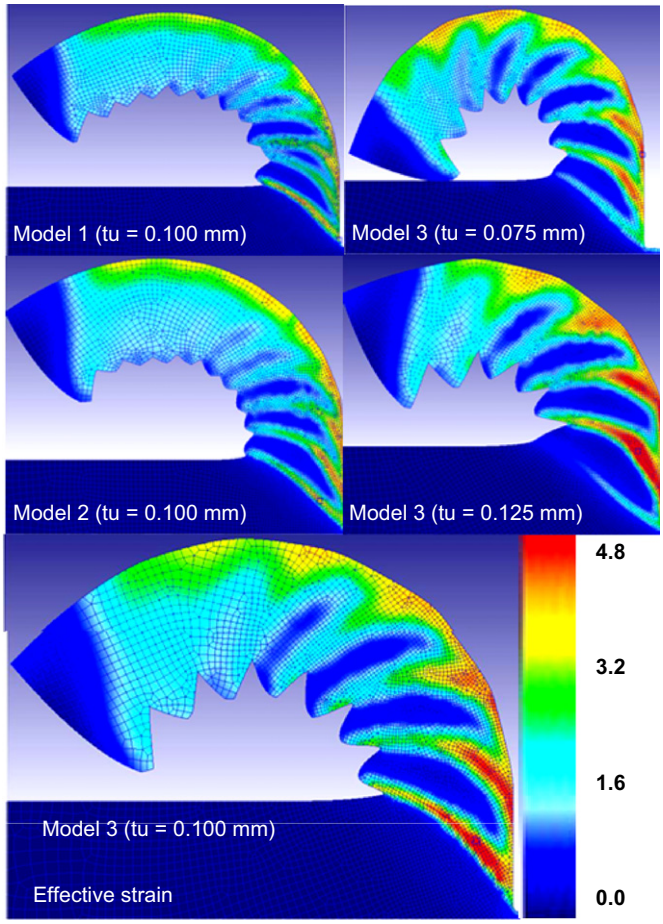

Fig. 19. Comparison of modified material models on serrated chip formation with adiabatic shearing (v_c =120 m/min, t_u=0.1 mm/rev, 0° rake angle, r_β= 5 mm).

two different rake angle, three different undeformed chip thickness values and two different cutting speeds.

The results reveal that material flow stress and finite element formulation greatly affects not only chip formation mechanism but also forces and temperatures predicted. Chip formation process for adiabatic shearing in machining Ti–6Al–4V alloys is

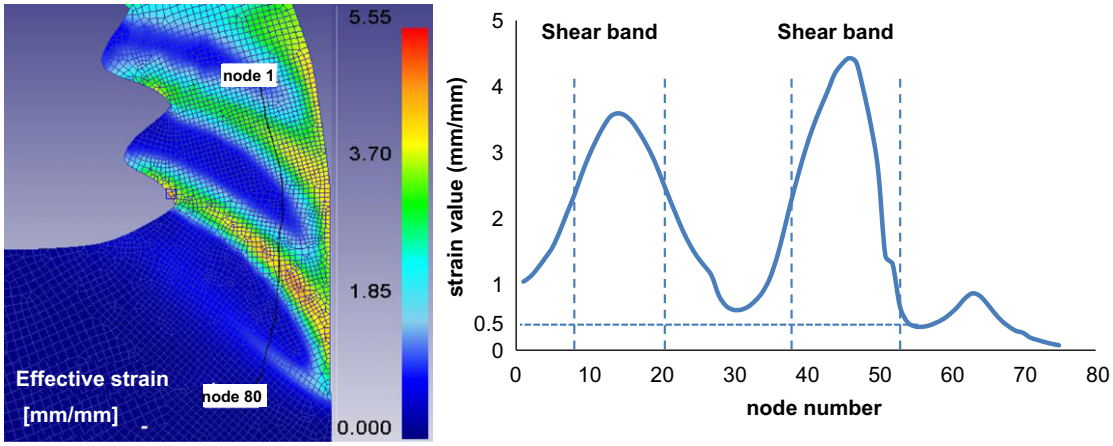

Fig. 20. Effective strain values along a path into the segmented chip with adiabatic shearing.

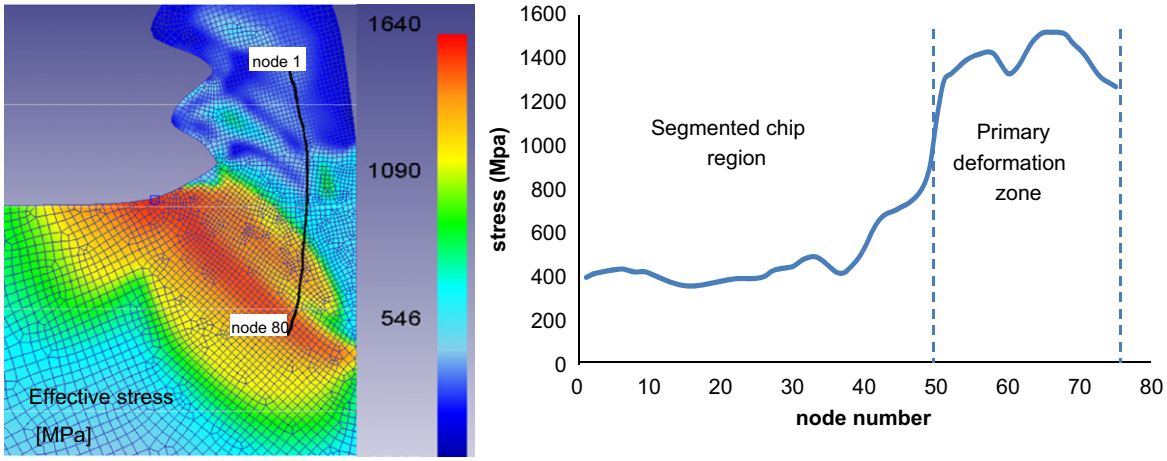

Fig. 21. Effective stress values along a path into the segmented chips.

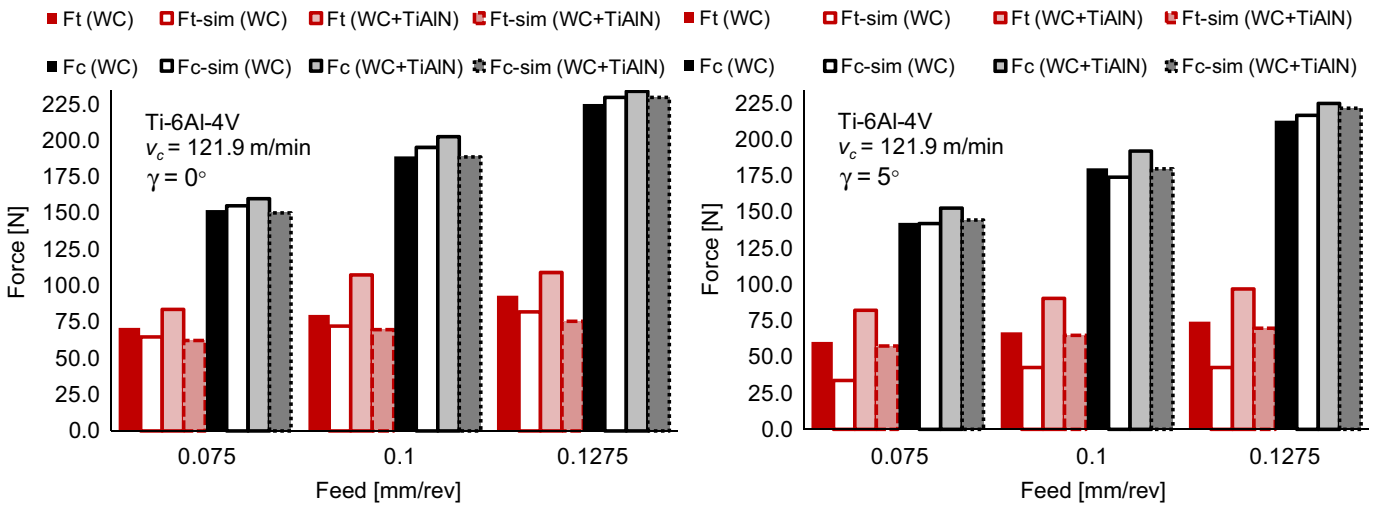

Fig. 22. Comparison of measured and simulated cutting forces.

Table 4
Comparison of predicted chip thickness and serrated pitch with experiments.

Tool	Rake angle, γ [°]	v_c (m/min)	t_u (mm)	Experimental			Simulation		
				t_{c_min}	t_{c_max}	p	t_{c_min}	t_{c_max}	p
Uncoated WC/Co	0	121.9	0.075	0.095	0.133	0.05	0.081	0.101	0.025
Uncoated WC/Co	0	121.9	0.1	0.13	0.192	0.07	0.108	0.135	0.045
Uncoated WC/Co	0	121.9	0.127	0.104	0.177	0.9	0.12	0.163	0.75
Uncoated WC/Co	0	240.8	0.1	0.087	0.16	0.08	0.107	0.137	0.035
Uncoated WC/Co	0	240.8	0.127	0.102	0.186	0.095	0.128	0.17	0.04
TiAlN coated WC/Co	0	121.9	0.1	0.137	0.182	0.075	0.107	0.135	0.035
TiAlN coated WC/Co	0	121.9	0.127	0.14	0.216	0.1	0.133	0.172	0.043
TiAlN coated WC/Co	5	121.9	0.1	0.102	0.158	0.073	0.107	0.134	0.034
TiAlN coated WC/Co	5	121.9	0.127	0.12	0.208	0.080	0.135	0.172	0.04
Uncoated WC/Co	5	121.9	0.127	0.156	0.23	0.089	0.135	0.171	0.039

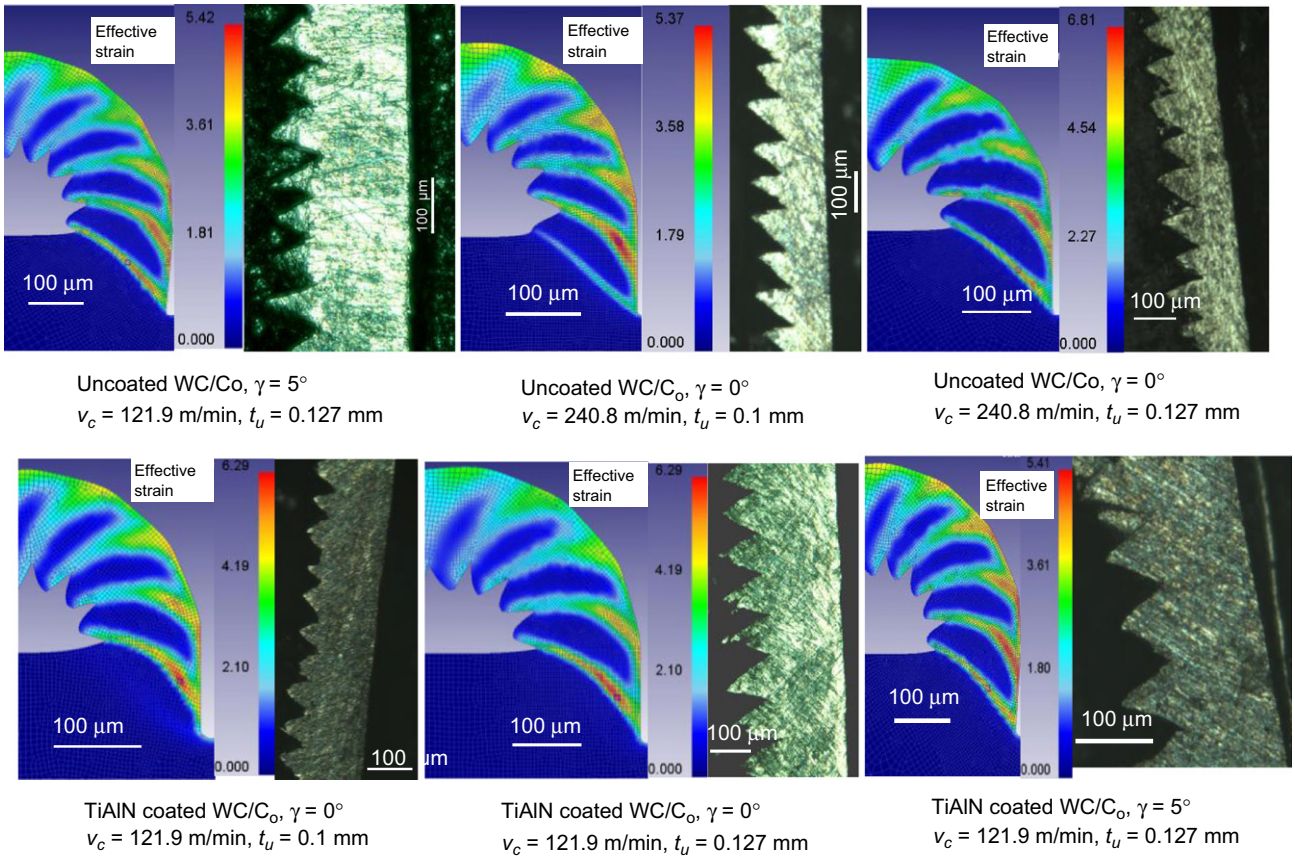

Fig. 23. Comparison of simulated serrated chip formation and captured chip images.

successfully simulated using finite element models without using damage models. The paper also demonstrates the importance of the work of Calamaz et al. [10] and emphasizes the importance of flow (strain) softening phenomenon during chip formation of titanium alloy Ti–6Al–4V independent of the FE software. It is also shown that FE simulations are reliable if the material properties and friction are defined properly in the chip formation process models. The following are specific conclusions can be drawn for this study:

- The cutting forces increase with increasing cutting speed and thrust forces decrease with decreasing rake angle.
- The degree of serration decreases while pitch of the serrated chips increases with decreasing cutting speed and increasing undeformed chip thickness and decreasing tool rake angle.
- TiAlN coated tools resulted in higher temperatures and higher cutting and thrust forces due to the larger edge radius.
- Flow softening is most effective between 300 and 700 °C and causes adiabatic shearing in the deformation zone during machining of Ti–6Al–4V alloy much lower than allotropic phase transformation (β-transus) temperature.
- Flow softening increases the degree of chip serration chip but produce more curved chips since strain-hardening effect weakens.

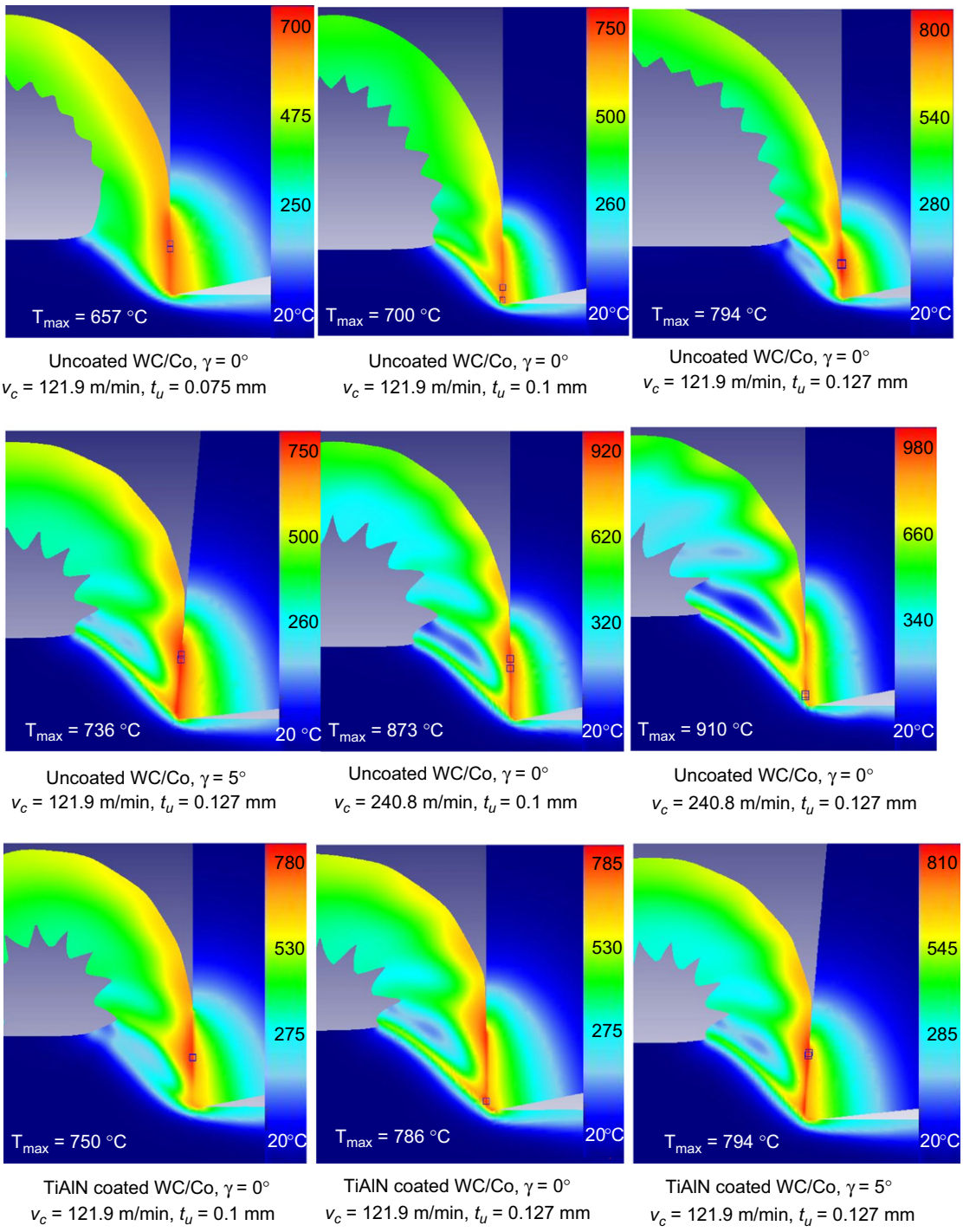

Fig. 24. Temperature distribution in simulated serrated chip formation.

Acknowledgements

The support for this project by the National Science Foundation (CMMI-0758820) is gratefully acknowledged. The authors are grateful to Dr. Anil K. Srivastava of TechSolve Inc., Cincinnati, Ohio for conducting orthogonal turning experiments.

References

[1] X. Yang, C.R. Liu, Machining titanium and its alloys, Machining Science and Technology 3 (1) (1999) 107–139.
[2] E.O. Ezugwu, Key improvements in the machining of difficult-to-cut aerospace superalloys, International Journal of Machine Tools and Manufacture 45 (2005) 1353–1367.
[3] A. Ginting, M. Nouari, Surface integrity of dry machined titanium alloys, International Journal of Machine Tools and Manufacture 49 (2009) 325–332.
[4] P.-J. Arrazola, A. Garay, L.M. Iriarte, M. Armendia, S. Marya, F. Le Maître, Machinability of titanium alloys (Ti6Al4V and Ti555.3), Journal of Materials Processing Technology 209 (5) (2009) 2223–2230.
[5] A. Gente, H.-W. Hoffmeister, Chip formation in machining Ti6Al4V at extremely high cutting speeds, CIRP Annals 50 (1) (2001) 49–52.
[6] A. Molinari, C. Musquar, G. Sutter, Adiabatic shear banding in high speed machining of Ti–6Al–4 V: experiments and modeling, International Journal of Plasticity 18 (2002) 443–459.
[7] R. Komanduri, B.-F. Turkovich, New observations on the mechanism of chip formation when machining titanium alloys, Wear 69 (1981) 179–188.

[8] R. Komanduri, Z.B. Hou, On thermoplastic shear instability in the machining of a titanium alloy, Metallurgical and Materials Transactions A 33A (2002) 2995–3010.
[9] M Cotterell, G Byrne, Dynamics of chip formation during orthogonal cutting of titanium alloy Ti–6Al–4V, CIRP Annals—Manufacturing Technology 57 (1) (2008) 93–96.
[10] M. Calamaz, D. Coupard, F. Girot, A new material model for 2D numerical simulation of serrated chip formation when machining titanium alloy Ti–6Al–4V, International Journal of Machine Tools and Manufacture 48 (2008) 275–288.
[11] S. Sun, M. Brandt, M.S. Dargusch, Characteristics of cutting forces and chip formation in machining of titanium alloys, International Journal of Machine Tools and Manufacture 49 (2009) 561–568.
[12] S. Nemat-Naser, W.G. Guo, V.F. Nesterenko, S.S. Indrankanti, Y.B. Gu, Dynamic response of conventional and hot isostatically presses Ti–6Al–4V alloys: experiments and modeling, Mechanics of Materials 33 (2001) 425–439.
[13] A. Vyas, M.C. Shaw, Mechanics of saw-tooth chip formation in metal cutting, ASME Journal of Manufacturing Science and Engineering 121 (2) (1999) 163–172.
[14] M. Baeker, J. Roesler, C. Siemers, Finite element simulation of segmented chip formation of Ti6Al4V, ASME Journal of Manufacturing Sciences and Engineering 124 (2002) 485–488.
[15] R.M. Miller, T.R. Bieler, S.L. Semiatin, Flow softening during hot working of Ti–6Al–4V with a lamellar colony microstructure, Scripta Materialia 40 (12) (1999) 1387–1393.
[16] R. Ding, Z.X. Guo, Microstructural evolution of a Ti–6Al–4V alloy during β-phase processing: experimental and simulative investigations, Materials Science and Engineering A365 (2004) 172–179.
[17] W.F. Cui, Z. Jin, A.H. Guo, L. Zhou, High temperature deformation behavior of $\alpha+\beta$-type biomedical Titanium alloy Ti–6Al–7Nb, Materials Science and Engineering A499 (2009) 252–256.
[18] D. Rittel, P. Landau, A. Venkert, Dynamic recrystallization as a potential cause for adiabatic shear failure, Physical Review Letters 101 (2008) 165501.
[19] T. Obikawa, E. Usui, Computational machining of titanium alloy—finite element modelling and a few results, Transactions of the ASME 118 (1996).
[20] R. Shivpuri, J. Hua, P. Mittal, A.K. Srivastava, Microstructure-mechanics interactions in modeling chip segmentation during titanium machining, CIRP Annals 51 (2001) 85–89.
[21] J. Hua, R. Shivpuri, Prediction of chip morphology and segmentation during the machining of titanium alloys, Journal of Materials Processing Technology 150 (2004) 124–133.
[22] D. Umbrello, Finite element simulation of conventional and high speed machining of Ti6Al4V alloy, Journal of Materials Processing Technology 196 (1–3) (2008) 79–87.
[23] T. Özel, S. Yildiz, J. Ciurana, Influence of material models on serrated chip formation in simulation of machining Ti–6Al–4V titanium alloy, in: Proceedings of the 12th CIRP International Workshop on Modeling of Machining Operations, San Sebastian, Spain, vol. 1, 2009, pp. 123–130.
[24] T. Özel, M. Sima, A.K. Srivastava, Finite element simulation of high speed machining Ti–6Al–4V alloy using modified material models, Transactions of the NAMRI/SME 38 (2010) 49–56.
[25] T. Özel, M. Sima, A.K. Srivastava, B. Kaftanoglu, Investigations on the effects of multi-layered coated inserts in machining Ti–6Al–4V alloy with experiments and finite element simulations, CIRP Annals—Manufacturing Technology 59 (1) (2010) 77–82.
[26] G.-R. Johnson, W.-H. Cook, A constitutive model for metals subjected to large strains, high strain rates and high temperatures, in: Proceedings of the Seventh International Symposium on Ballistics, Hague, Netherlands, vol. 54, 1983, pp. 1–7.
[27] D.-J. Bammann, M.-L. Chiesa, G.-C. Johnson, Modeling large deformation and failure in manufacturing processes, Theoretical and Applied Mechanics (1996) 359–376.
[28] K. Maekawa, T. Shirakashi, E. Usui, Flow stress of low carbon steel at high temperature and strain rate (Part 2), Bulletin of the Japan Society of Precision Engineering 17 (3) (1983) 167–172.
[29] S. Nemat-Nasser, J.-B. Isaacs, Direct measurement of isothermal flow stress of metals at elevated temperatures and high strain rates with application to Ta and Ta–W alloys, Acta Materialia 45 (1997) 907–919.
[30] Y.-B. Guo, Q. Wen, K.-A. Woodbury, Dynamic material behavior modeling using internal state variable plasticity and its application in hard machining simulations, ASME Journal of Manufacturing Science and Engineering 128 (2006) 749–756.
[31] W.-S. Lee, C.-F. Lin, High-temperature deformation behavior of Ti6Al4V alloy evaluated by high strain-rate compression tests, Journal of Materials Processing Technology 75 (1998) 127–136.
[32] W.-S. Lee, C.-F. Lin, Plastic deformation and fracture behavior of Ti–6Al–4V alloy loaded with high strain rate under various temperatures, Materials Science and Engineering A241 (1998) 48–59.
[33] H.W. Meyer, D.S. Kleponis, Modeling the high strain rate behavior of titanium undergoing ballistic impact and penetration, International Journal of Impact Engineering 26 (2001) 509–521.
[34] G. Kay, Failure modelling of titanium 6Al–4V and aluminum 2024-T3 with the Johnson–Cook material model, U.S. Lawrence Livermore National Laboratory, Report DOT/FAA/AR-03/57, 2003.
[35] S. Seo, O. Min, H. Yang, Constitutive equation for Ti–6Al–4 V at high temperatures measured using the SHPB technique, International Journal of Impact Engineering 31 (2005) 735–754.
[36] U. Andrade, M. Meyers, K Vecchio, A. Chokshi, Dynamic recrystallization in high-strain, high-strain-rate plastic deformation of copper, Acta Metallurgica et Materialia 42 (1994) 3183–3195.
[37] S. Anurag, Y.-B. Guo, A modified micromechanical approach to determine flow stress of work materials experiencing complex deformation histories in manufacturing processes, International Journal of Mechanical Sciences 49 (7) (2007) 909–918.
[38] J. Sun, Y.-B. Guo, Material flow stress and failure in multiscale machining titanium alloy Ti6Al4V, International Journal of Advanced Manufacturing Technology 41 (2009) 651–659.
[39] T. Özel, Influence of friction models on finite element simulations of machining, International Journal of Machine Tools and Manufacture 46 (5) (2006) 518–530.
[40] Y. Karpat, T. Özel, Mechanics of high speed cutting with curvilinear edge tools, International Journal of Machine Tools and Manufacture 48 (2008) 195–208.
[41] M. Calamaz, Etude des mécanismes d'endommagement des outils carbure WC-Co par la caractérisation de l'interface outil-copeau—Application à l'usinage de l'alliage de titane aéronautique TA6V", Ph.D. Thesis, Université de Bordeaux, France, No. 2008-3605, June 2008.